# Implicit Large Eddy Simulation
# of Transitional Flows Over Airfoils and Wings

Alejandra Uranga[*]

*Massachusetts Institute of Technology, Cambridge, MA 02139, U.S.A.*

Per-Olof Persson[†]

*University of California Berkeley, Berkeley, CA 94720 U.S.A.*

Mark Drela[‡] and Jaime Peraire[§]

*Massachusetts Institute of Technology, Cambridge, MA 02139, U.S.A.*

The present work aims at predicting the formation of laminar separation bubbles (LSB) and the related transition to turbulence by means of Implicit Large Eddy Simulations with a high-order Discontinuous Galerkin (DG) method. We focus on the flow around an SD7003 rectangular wing section at an angle of attack of $4^o$ degrees and consider two different Reynolds numbers of 10,000 and 60,000 in order to gain insight into the characteristics of the laminar and turbulent regimes. At Reynolds number 10,000 the flow remains laminar and essentially two dimensional over the wing surface, and only the wake appears to exhibit a turbulent behavior. For the case at Reynolds 60,000, the flow is unsteady over the upper wing surface and the time averaged streamlines show a separation bubble which starts at about 24% of the chord. A close to 51% of the chord, the flow is fully turbulent. These findings appear to be in agreement with previously published results despite the relatively coarse meshes employed, which suggest that the DG method used is particularly suited to simulate these flows. Finally, transition is found to be caused by unstable Tollmien-Schlichting (TS) waves, as revealed by the growth of the stream-wise amplification factor.

## Nomenclature

**Letters**

| | | | |
|---|---|---|---|
| $c$ | Airfoil chord | $U_\infty$ | Free-stream flow speed |
| $C_D$ | Drag coefficient | $\bar{u}^*$ | Pseudo-velocity profile |
| $C_{fs}$ | Stream-wise skin friction coefficient | $u_i$ | Velocity component in direction $x_i$ |
| $C_L$ | Lift coefficient | $u_s$ | Stream-wise velocity component, |
| $C_p$ | Pressure coefficient | $u_t$ | Transverse velocity component |
| $E$ | Total energy | $u_z$ | Cross-flow (span-wise) velocity component |
| $h_b$ | Separation bubble height | $x_i$ | Computational coordinate $i$ |
| $p$ | Static pressure | $x_r$ | Reattachment location |
| $Pr$ | Prandtl number, $Pr = \mu\,c_p/\kappa$ | $x_{sep}$ | Separation location |
| $Re$ | Free-stream Reynolds number, $Re = U_\infty c/\nu$ | $x_{tr}$ | Transition location |
| $t$ | Physical time | $x$ | Chord-wise direction |
| $t^*$ | Non-dimensional time, $t^* = t\,U_\infty/c$ | $y$ | Direction perpendicular to the chord-wise and span-wise directions |

[*]Ph.D. Candidate, Dept. of Aeronautics and Astronautics, 77 Massachusetts Avenue Room 37-442, Cambridge, MA 02139, auranga@mit.edu, AIAA Student Member.

[†]Assistant Professor, Department of Mathematics, AIAA Member.

[‡]Terry J. Kohler Professor of Fluid Dynamics, Dept. of Aeronautics and Astronautics, AIAA Fellow.

[§]Professor, Dept. of Aeronautics and Astronautics, AIAA Associate Fellow.

American Institute of Aeronautics and Astronautics

| $z$ | Span-wise direction |

**Symbols**

| | |
|---|---|
| $\alpha$ | Angle of attack |
| $\gamma$ | Fluid specific heat ratio |
| $\delta_1^*$ | Stream-wise boundary layer displacement thickness |
| $\Delta t^*$ | Non-dimensional time step $\Delta t^* = \Delta t\, U_\infty/c$ |
| $\mu$ | Dynamic viscosity coefficient |
| $\nu$ | Kinematic viscosity coefficient $\nu = \mu/\rho$ |
| $\rho$ | Fluid density |
| $\theta_{11}$ | Stream-wise boundary layer momentum thickness |

**Subscripts**

| | |
|---|---|
| $i$ | In the direction of coordinate $x_i$ |
| $r$ | Reattachment |
| $s$ | In the free-stream direction, *i.e.* stream-wise |
| $sep$ | Separation |
| $t$ | In the transverse direction, *i.e.* perpendicularly to both free-stream and span-wise directions |
| $tr$ | Transition |
| $z$ | In the cross-flow direction, *i.e.* span-wise |

# I.  Introduction

ACCURATELY predicting transition to turbulence is of crucial importance for the simulation of low Reynolds number flows since in these regimes the transition location has a significant impact on aerodynamic performance. This is primarily due to the fact that laminar flows have a much greater tendency to separate than the essentially turbulent flows encountered at high Reynolds numbers. In the presence of an adverse pressure gradient, a laminar boundary layer can separate and subsequently reattach, thus forming what is known as a laminar separation bubble (LSB).

Several studies[1,2] have shown that transition to turbulence can be predicted by means of Large Eddy Simulations (LES), and this type of simulation can significantly benefit from the use high-order methods due to the high computational cost involved. Furthermore, simulation of transition requires low numerical dispersion and dissipation, and therefore the use high-order methods seems to be a practical requirement. Here, we have chosen to use a high-order Discontinuous Galerkin (DG) Finite Element method as it combines high accuracy with the geometric flexibility required for practical applications. To the author's knowledge, the present investigation is the first attempt at using a DG method for Large Eddy Simulations.

The present work aims at predicting the formation of an LSB and the related transition to turbulence. We focus on the flow around an SD7003 rectangular wing section at an angle of attack of $4°$, and consider Reynolds numbers of 10,000 and of 60,000 in order to gain insight into the characteristics of both laminar and turbulent regimes. This case is chosen since the flow exhibits a fairly stable LSB on the upper surface, and extensive experimental data is available for comparison,[3] as well as numerical simulations.[2] Furthermore, this flow regime corresponds to the one encountered in small flying animals and in micro-air vehicles (MAV's).

# II.  Computational Methodology

## A.  Governing Equations and Turbulence Modeling

The motion of a compressible Newtonian fluid is governed by the Navier-Stokes equations which express the conservation of mass, momentum and energy,

$$\frac{\partial \rho}{\partial t} + \frac{\partial}{\partial x_i}\left(\rho u_i\right) = 0 \tag{1}$$

$$\frac{\partial}{\partial t}\left(\rho u_i\right) + \frac{\partial}{\partial x_j}\left(\rho u_i u_j\right) = -\frac{\partial p}{\partial x_i} + \frac{\partial \tau_{ij}}{\partial x_j} \quad \text{for } i \in \{1,2,3\} \tag{2}$$

$$\frac{\partial}{\partial t}(\rho E) + \frac{\partial}{\partial x_j}\left[u_j\left(\rho E + p\right)\right] - \frac{\partial}{\partial x_j}\left(u_i \tau_{ji}\right) + \frac{\partial q_j}{\partial x_j} = 0 \tag{3}$$

where the viscous stress tensor, $\tau_{ij}$, and the heat flux, $q_i$, are defined by, respectively,

$$\tau_{ij} \equiv \mu\left[\left(\frac{\partial u_i}{\partial x_j} + \frac{\partial u_j}{\partial x_i}\right) - \frac{2}{3}\frac{\partial u_k}{\partial x_k}\delta_{ij}\right] \tag{4}$$

$$q_j = -\frac{\mu}{Pr}\frac{\partial}{\partial x_j}\left(E + \frac{p}{\rho} - \frac{1}{2}u_k u_k\right)\ . \tag{5}$$

American Institute of Aeronautics and Astronautics

In the above equations, $\rho$ denotes the fluid density, $u_i$ is the velocity component in the direction $x_i$, $p$ is the static pressure, $E$ is the total energy, $\mu$ the dynamic viscosity coefficient, and $Pr$ the flow Prandtl number. In order to close the system, we use the ideal gas equation of state written in the form

$$p = (\gamma - 1)\rho \left( E - \frac{1}{2} u_k u_k \right) . \tag{6}$$

For all the flows considered the specific heat ratio is $\gamma = 1.4$, the Prandtl number is $Pr = 0.72$, the free stream Mach number is 0.2, and kinematic viscosity, $\nu = \mu/\rho$, is assumed to be constant since were are only considering low Mach number flows.

In a Large-Eddy Simulation (LES), the large-scale motions are resolved while the small scales are modeled through a sub-grid-scale model. The principle behind LES is justified by the fact that the larger scales, because of their size and strength, carry most of the flow energy while being responsible for most of the transport, and therefore should be simulated precisely (*i.e.* resolved). On the other hand, the small scales have relatively little influence on the mean flow and thus can be approximated (*i.e.* modeled). Furthermore, small scales tend to be more homogeneous and isotropic and hence are easier to model than the large scales, thus ensuring higher accuracy of the overall simulations.

In the present work we follow the Implicit Large Eddy Simulation (ILES) approach, and hence the unresolved small eddies are accounted for by means of the numerical dissipation and no sub-grid-scale model is employed such that the full (unfiltered) compressible Navier-Stokes equations are solved. This approach has been successfully used by Visbal and collaborators[2] using a compact difference method for the simulation of the flow around an SD7003 airfoil.

## B. High-Order Discontinuous Galerkin Method and Time Stepping Scheme

The modeling equations are solved using a high-order Discontinuous Galerkin method implemented in the computational code *3DG*. This framework solves time-dependent systems of conservation laws of the form,

$$\begin{cases} \dfrac{\partial u}{\partial t} + \nabla \cdot F_i(u) - \nabla \cdot F_v(u, q) = S(u, q) \\ q - \nabla u = 0 \end{cases} \tag{7}$$

in a domain $\Omega$, with conserved state variables $u$, inviscid flux function $F_i$, viscous flux function $F_v$, and source term $S$.

We consider a triangulation $\mathcal{T}_h$ of the spatial domain $\Omega$ and introduce the finite element spaces $V_h$ and $\Sigma_h$ as

$$\begin{aligned} V_h &= \{ v \in [L^2(\Omega)]^m \mid v|_K \in [\mathcal{P}_p(K)]^m, \ \forall K \in \mathcal{T}_h \} , \\ \Sigma_h &= \{ r \in [L^2(\Omega)]^{dm} \mid r|_K \in [\mathcal{P}_p(K)]^{dm}, \ \forall K \in \mathcal{T}_h \} , \end{aligned}$$

where $\mathcal{P}_p(K)$ is the space of polynomial functions of degree at most $p \geq 0$ on triangle $K$, $m$ is the dimension of $u$ and $d$ is the spatial dimension.

The DG formulation is of the form: find $u_h \in V_h$ and $q_h \in \Sigma_h$ such that for all $K \in \mathcal{T}_h$,

$$\int_K q_h \cdot r \, dx = -\int_K u_h \nabla \cdot r \, dx + \int_{\partial K} \hat{u} r \cdot n \, ds , \qquad \forall r \in [\mathcal{P}_p(K)]^{dm},$$

$$\int_K \frac{\partial u_h}{\partial t} v \, dx - \int_K [F_i(u_h) - F_v(u_h, q_h)] \cdot \nabla v \, dx$$

$$= \int_K S(u_h, q_h) v \, dx - \int_{\partial K} [\hat{F}_i - \hat{F}_v] \cdot n v \, ds , \qquad \forall v \in [\mathcal{P}_p(K)]^m.$$

Here, the numerical fluxes $\hat{F}_i$, $\hat{F}_v$ and $\hat{u}$ are approximations to $F_i$, $F_v$ and $u$, respectively, on the boundary $\partial K$ of the element $K$. The DG formulation is complete once these numerical fluxes are specified in terms of $q_h$ and $u_h$ and the boundary conditions.

The inviscid flux is determined using Roe's scheme[4] whereas the viscous flux is calculated using the Compact Discontinous Galerkin (CDG) method introduced by Peraire & Persson.[5] By choosing the numerical flux $\hat{u}$ to be a function of $u_h$ and not $q_h$, the additional $q_h$ variables can be eliminated after discretization at

American Institute of Aeronautics and Astronautics

element level. This results in a system involving only the degrees of freedom corresponding to the conserved variables $u_h$. The final result is a system of coupled ordinary differential equations of the form,

$$\boldsymbol{M}\dot{\boldsymbol{u}} = \boldsymbol{R}(\boldsymbol{u}) \ , \tag{8}$$

where $\boldsymbol{u}(t)$ is a vector containing the degrees of freedom associated with $u_h$, and $\dot{\boldsymbol{u}}$ denotes the time derivative of $\boldsymbol{u}(t)$. Here, $\boldsymbol{M}$ is the mass matrix, while $\boldsymbol{R}$ is the residual vector which is a nonlinear function of $\boldsymbol{u}$. We use nodal basis expansions to represent $u_h$ inside each element.

The linear systems of equations are solved with a combination of incomplete factorizations (ILU) and p-multigrid with Newton-GMRES preconditioning following the work by Persson & Peraire.[7] The code is parallelized with block-incomplete LU factorizations, the details of which can be found in the paper by Persson.[6]

Finally, the system is solved using the third order diagonal implicit Runge-Kutta (DIRK) method.[8] This allows to take large time steps, and hence the time step is chosen only based on physical time resolution considerations and not on numerical stability factors. A non-dimensional times step of $\Delta t^* = \Delta t \times U_\infty/c = 0.01$ was used, and the solution was recorded every 10 steps for computing statistics.

The average fields and velocity correlations are computed by averaging the solution after the initial transient has passed, as estimated by looking at the forces on the wing, and are performed over a non-dimensional time interval of around 8.

## C.   Computational Grids

The flow around a rectangular wing with an SD7003 airfoil profile at an angle of attack of $4°$ is considered. The wing span to chord ratio is set to 0.2, following the findings of Galbraith and Visbal.[2] The axes are setup with $x$ being the chord-wise direction and $z$ the span-wise direction, such that the leading-edge is located along the line $x = 0$, $y = 0$.

Measured from the wing's leading-edge line, the domain extends 4.3 chord lengths upstream, 7.4 chord lengths downstream, 5.9 chord lengths above, and 6.0 chord lengths below. Thus, if we denote by $c$ the chord
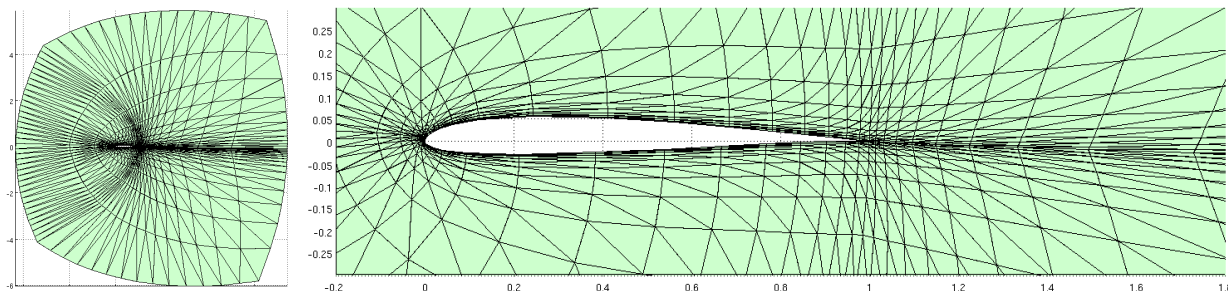


**Figure 1.   View of a span-wise plane of the coarse grid (grid 1): (left) domain, (right) closer view on foil. This grid has 430,080 degrees-of-freedom in 21,504 tetrahedral elements.**
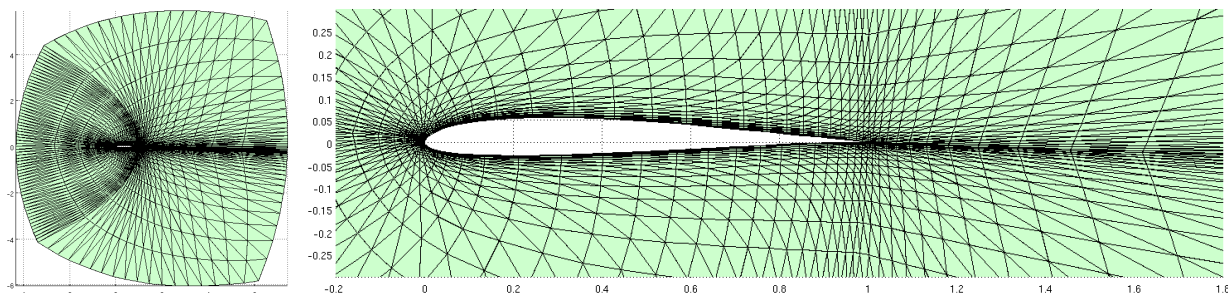


**Figure 2.   View of a span-wise plane of the medium grid (grid 2): (left) domain, (right) closer view on foil. This grid has 1,056,000 degrees-of-freedom in 52,800 tetrahedral elements.**

American Institute of Aeronautics and Astronautics

length, the domain spans on the range [-4.3c , 7.4c] × [-6.0c , 5.9c] × [0 , 0.2c] along the chord-wise, vertical, and span-wise directions, respectively.

The computational domain has periodic boundary conditions along the span-wise direction in order to simulate an infinite wing. The wing's surface is represented by a non-slip, adiabatic, boundary condition, while a full-state type boundary condition is imposed at the far-field of the computational domain.

In order to investigate how much spatial resolution is needed to capture the transition to turbulence that occurs in the separation bubble, two computational grids are considered: a coarse grid (hereafter referred to as grid 1) with 21,504 tetrahedral elements, and a medium grid (grid 2) with 52,800 tetrahedral elements. Third-order polynomials are employed, which result in a fourth-order accurate method in space; thus, grids 1 and 2 have 430,080 and 1,056,000 degrees-of-freedom, respectively. Figures 1 and 2 show the coarse and medium computational grids on a planar cut along the span-wise direction.

## D.    Angle of Attack for Comparisons with XFoil

The Navier-Stokes methods apply the specified freestream angle $\alpha = 4°$ at the outer grid inflow boundary, without accounting for the 2D vortex farfield of the airfoil. The missing vortex upwash at the inlet gives a decrease in the effective angle of attack seen by the airfoil by the amount

$$\Delta\alpha = -\frac{C_L}{4\pi\, r/c}$$

where $C_L$ is the airfoil lift coefficient and $r/c$ is the distance-to-chord ratio between the inlet boundary and the wing's lift centroid (or center of pressure), such that the higher-order $y$-doublet farfield term is exactly zero. For the current case of $C_L = 0.6$, $r/c = 6$, the correction is $\Delta\alpha = -0.46°$. Since XFoil fully accounts for the farfield vortex, it was therefore run with the smaller angle

$$\alpha_{\text{XFoil}} = 4° - 0.46° = 3.54°$$

to give a more correct comparison to the Navier-Stokes results. Furthermore, the critical amplification factor was set to $N_{crit} = 7.5$, since for this value the transition occurs at a location consistent with the present LES results.

## E.    Q-Criterion

Dubeif and Delcayre[9] proposed what is referred to as the $q$-criterion as a way of identifying vortical coherent structures. It is defined as

$$Q = \frac{1}{2}\left(\Omega_{ij}\Omega_{ij} - S_{ij}S_{ij}\right) = \frac{1}{4}\left(\omega^2 - 2S_{ij}S_{ij}\right) = \frac{1}{2}\frac{\nabla^2 p}{\rho} \tag{9}$$

where the $\Omega_{ij}$ and $S_{ij}$ are the anti-symmetric and symmetric part of the velocity gradient respectively, that is

$$\Omega_{ij} \equiv \frac{1}{2}\left(\frac{\partial u_i}{\partial x_j} - \frac{\partial u_j}{\partial x_i}\right) \quad \text{and} \quad S_{ij} \equiv \frac{1}{2}\left(\frac{\partial u_i}{\partial x_j} + \frac{\partial u_j}{\partial x_i}\right)\ .$$

The $q$-criterion thus represents the balance between the rate of vorticity $\Omega^2 = \Omega_{ij}\Omega_{ij}$ and the rate of strain $S^2 = S_{ij}S_{ij}$. In the core of a vortex, $q > 0$ since vorticity increases as the center of the vortex is approached. Thus regions of positive q-criterion correspond to vortical structures.

## F.    Boundary Layer Parameters

In order to obtain the boundary layer parameters, we first obtain the pseudo-velocity profile by integrating the vorticity, namely

$$\vec{u}^*(n) = \int_0^n \vec{\omega} \times \hat{n}\, dn\ . \tag{10}$$

Here $\vec{u}^*$ denotes the pseudo-velocity, $\vec{\omega}$ the flow vorticity vector, $\hat{n}$ the unit vector normal to the airfoil at the location considered, and $n$ the local coordinate along the direction normal to the foil. The reason for using this pseudo-velocity profile is that it always asymptotes outside the boundary layer, even with strong curvature, thus making the edge of the boundary layer a well defined quantity.

American Institute of Aeronautics and Astronautics

The edge $n_e$ of the boundary layer is then taken to be the location where *both* the magnitudes of vorticity, $|\vec{\omega}|$, and of vorticity variation along the normal, $|d\vec{\omega}/dn|$, are below a certain threshold, namely

$$|\vec{\omega}|\, n \quad < \quad \epsilon_0 |\vec{u}^*| \tag{11}$$

$$\left|\frac{d\vec{\omega}}{dn}\right| n^2 \quad < \quad \epsilon_1 |\vec{u}^*| \ . \tag{12}$$

The edge velocity is then $\vec{u}_e^* = \vec{u}^*\,(n_e)$, with magnitude $u_e = |\vec{u}_e^*|$.

We then define the local stream-wise and transverse unit vectors as, respectively,

$$\hat{s}_1 = \vec{u}_e/u_e \quad \text{and} \quad \hat{s}_2 = \hat{s}_1 \times \hat{n} \ , \tag{13}$$

Thus, the stream-wise and cross-flow velocity profiles are given by, respectively,

$$u_1(n) = \vec{u}^*(n) \cdot \hat{s}_1 \quad \text{and} \quad u_2(n) = \vec{u}^*(n) \cdot \hat{s}_2 \ . \tag{14}$$

The boundary layer stream-wise displacement and momentum thicknesses are then

$$\delta_1^* = \int_0^{n_e} \left(1 - \frac{u_1}{u_e}\right) dn \tag{15}$$

$$\theta_{11} = \int_0^{n_e} \left(1 - \frac{u_1}{u_e}\right) \frac{u_1}{u_e}\, dn \tag{16}$$

with the shape factor

$$H_1 = \delta_1^*/\theta_{11} \ . \tag{17}$$

## III.   Flow Around a Rectangular Wing

### A.   Laminar Regime

At a Reynolds number of 10,000 the flow is found to be fundamentally two-dimensional with little variation along the spanwise direction and close-to-periodic vortex shedding, as can be seen in the time history of lift and drag force coefficients for grid 1 in Figure 3. The average lift coefficient is 0.3826, and the average drag coefficient is 0.0504 when using the medium grid 2. The average forces obtained on grid 1 differ by less than 0.2% from those obtained with grid 2 (0.3833 and 0.0503 respectively for lift and drag coefficients), thus indicating that the spatial resolution provided by grid 2 is sufficient to capture the main flow features at this Reynolds number.

The average pressure and stream-wise skin friction coefficients are shown in Figure 4. The comparison with a two-dimensional simulation performed on a grid with the same resolution than a span-wise plane is shown in the figures. Both the time evolution of the force and the average stress coefficients obtained with three-dimensional simulations are very close to the two-dimensional results, which confirms that the flow at a Reynolds number of 10,000 and 4° angle of attack is fundamentally two dimensional.

At this Reynolds number, the flow is found to be laminar all over the airfoil. The boundary layer separates at a distance of 0.34 chords from the leading edge, and does not reattach. This can be seen in the instantaneous and average span-wise vorticity contours on the plane at the middle of the wing ($y = 0.1$) as shown in Figure 5, on the friction coefficient distribution of Figure 4, and on the average stream-lines shown in Figure 9. The iso-surfaces of q-criterion of Figure 7 also indicate that the flow remains laminar until close to the trailing edge where the boundary layers generated by the upper and lower surfaces meet.

The stream-wise displacement thickness $\delta_{*1}$, momentum thickness $\theta_1$, and shape factor $H_1 = \delta_{*1}/\theta_1$ of Figure 10 confirm that transition to turbulence occurs aft of the trailing edge. The dashed line shows the XFoil prediction.

American Institute of Aeronautics and Astronautics

**Table 1. SD7003 at Reynolds 10,000 and $4°$ angle of attack using grid 2.**

| Source | Freestream Turbulence $Tu$ | Separation $x_{sep}/c$ | Transition $x_{tr}/c$ | Reattachment $x_r/c$ | $\overline{C_L}$ | $\overline{C_D}$ |
|---|---|---|---|---|---|---|
| XFoil[10] | $(N_{crit} = 7.5)$ | 0.32 | - | - | 0.2735 | 0.0461 |
| present ILES | 0 | 0.34 | - | - | 0.3826 | 0.0504 |
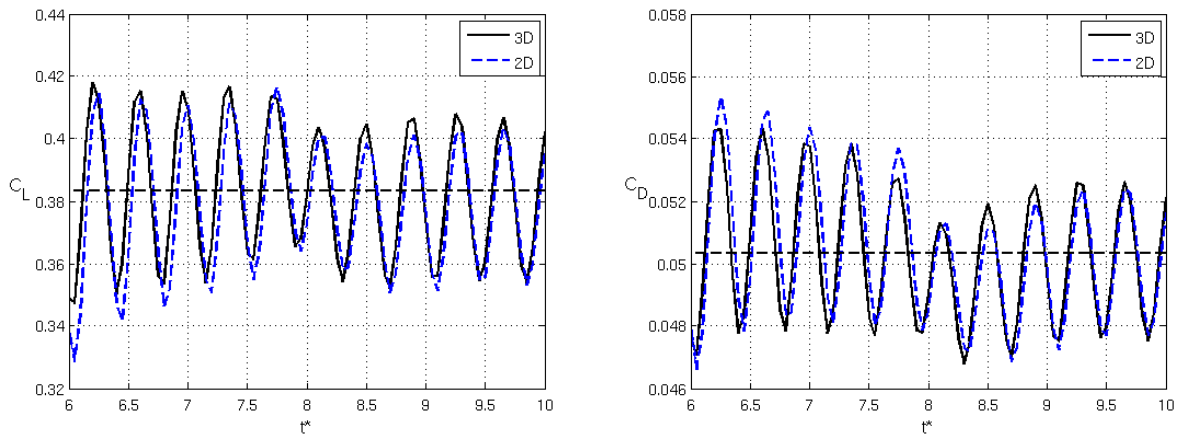


**Figure 3. Time variation of lift coefficient (left) and drag coefficients (right) at $Re = 10{,}000$: 2D versus 3D simulations. The dotted horizontal line indicates the average value.**
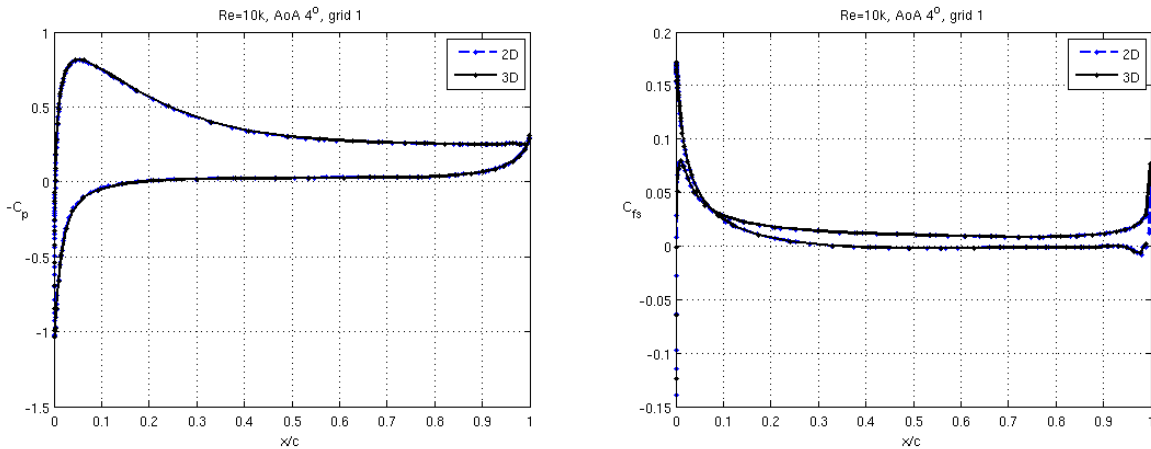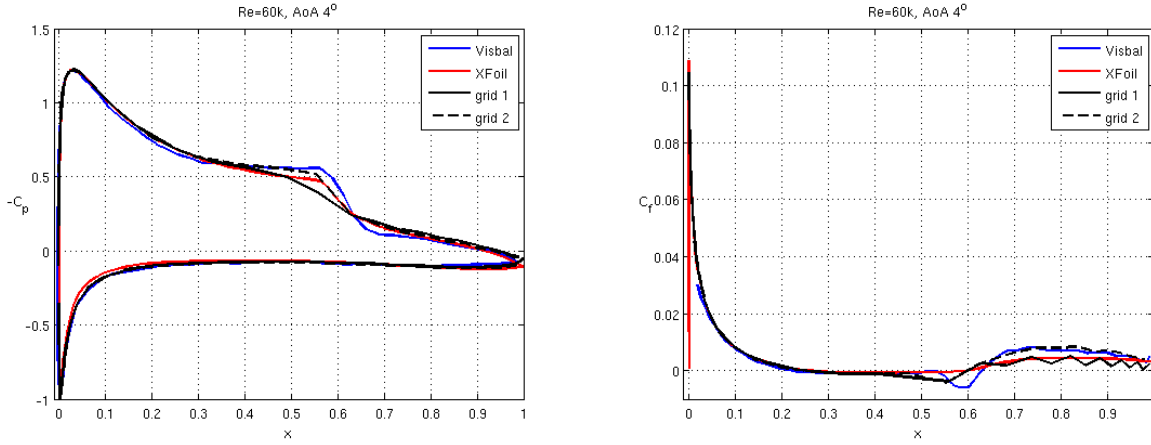


**Figure 4. Average pressure coefficient (left) and stream-wise skin friction coefficient (right) at $Re = 10{,}000$: 2D versus 3D simulations.**
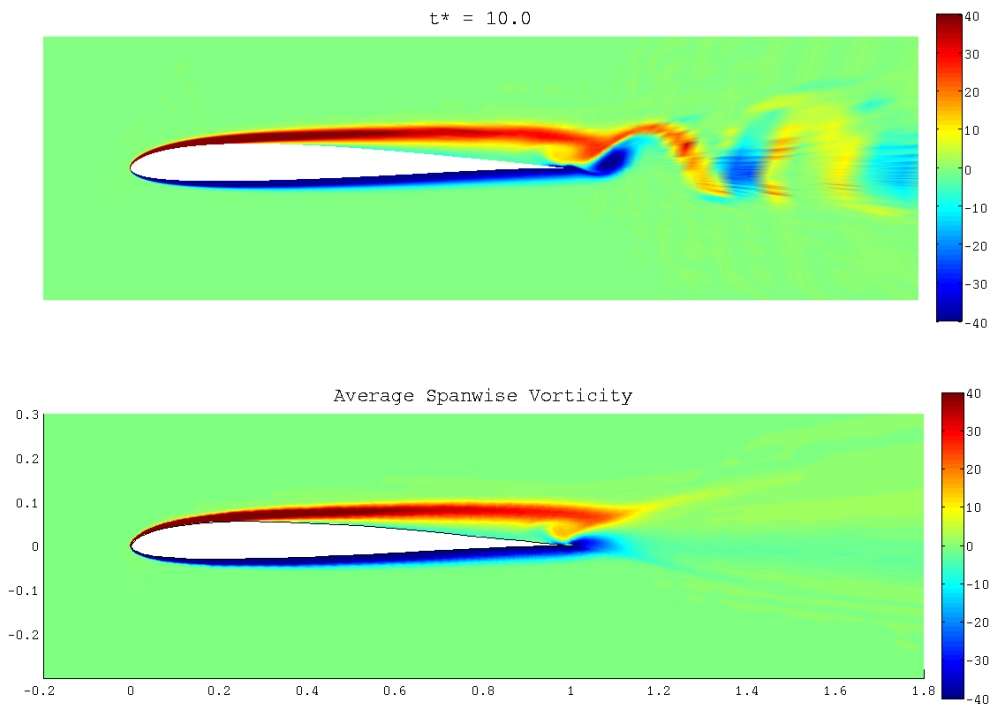
**Figure 5. Span-wise vorticity on the plane at the middle of the wing at $Re = 10{,}000$: instantaneous (top) and average (bottom) contours.**
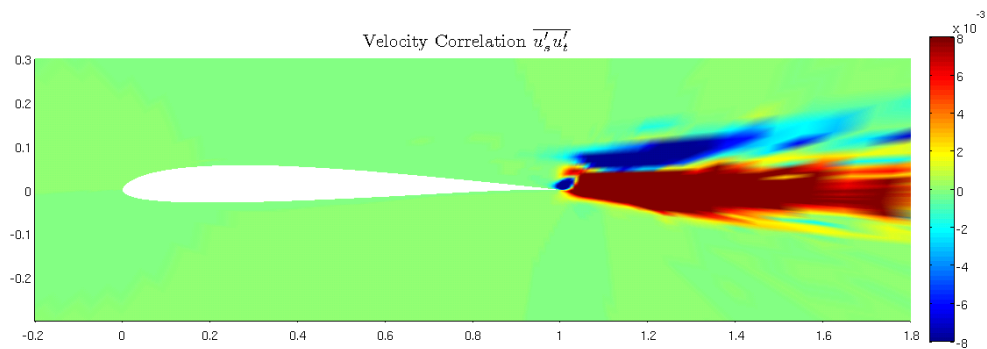


**Figure 6. Average non-dimensional velocity correlations $\overline{u'_s u'_t}/U^2_\infty$ at $Re = 10{,}000$.**
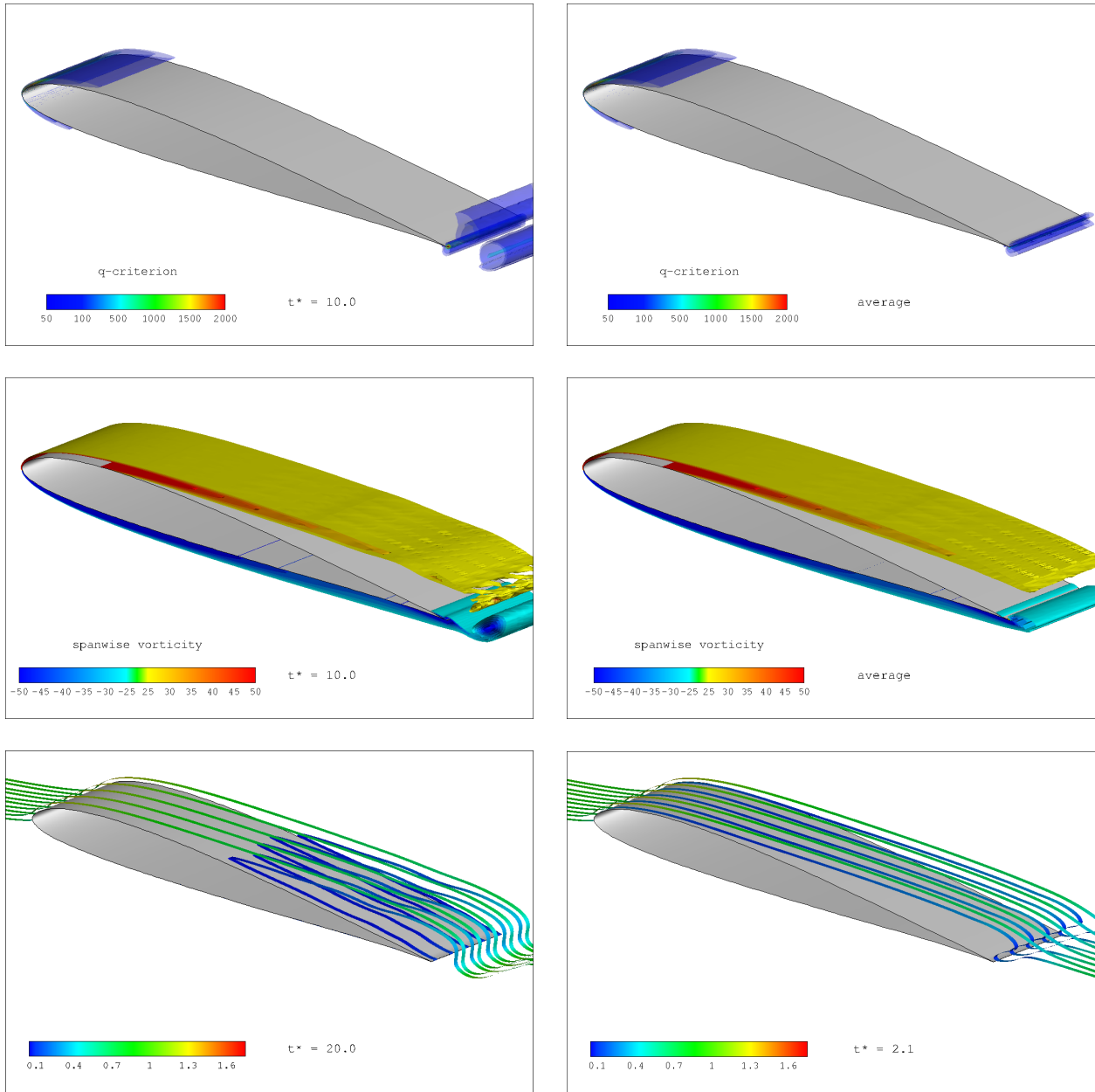
**Figure 7.** Instantaneous (left) and average (right) iso-surfaces of q-criterion (top) and span-wise vorticity (middle) at $Re = 10,000$.

American Institute of Aeronautics and Astronautics
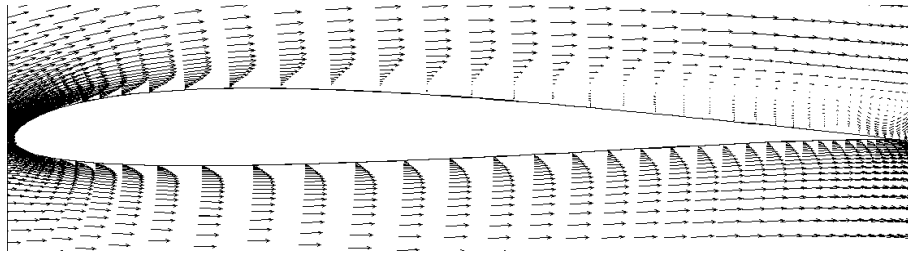
Figure 8. Average velocity vectors on the midplane at $Re = 10,000$.
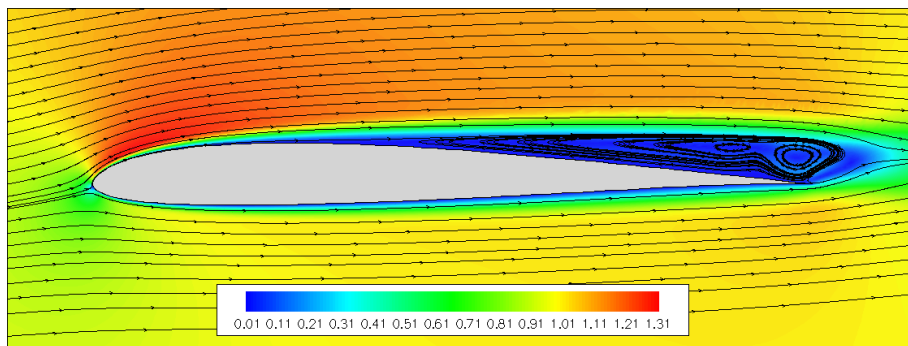


Figure 9. Average steamlines on the midplane at $Re = 10,000$. The colored contours show velocity magnitude.
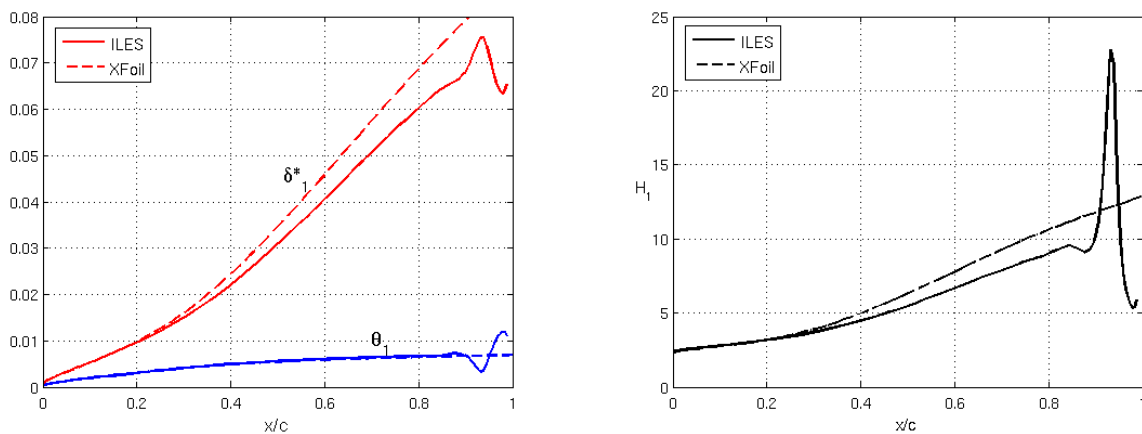


Figure 10. Boundary layer average displacement and momentum thicknesses (left), and shape factor (right) evolution along the stream-wise direction on the midplane at $Re = 10,000$. The dashed lines show XFoil's prediction.

**Figure 11.** Average pressure coefficient (left) and stream-wise skin friction coefficient (right) at $Re = 60,000$: comparison of results using coarse (grid 1) and medium (grid 2) spatial resolutions.

## B.   Turbulent Regime

### 1.  Spatial Resolution

The comparison of average pressure coefficient and skin friction coefficient on the airfoil obtained with the coarse and medium grids can be seen in Figure 11. The coarse mesh is unable to properly capture the separation bubble and associated transition to turbulence.

### 2.  Results with Medium Grid

At a Reynolds number of 60,000, three-dimensional structures are present as made visible by contours of vorticity or q-criterion presented in Figure 17. With a fourth-order method, a relatively coarse mesh with one million degrees-of-freedom is able to accurately capture the transition location, the position of separation and reattachment, as well as the average pressure and skin friction coefficient profiles along the foil.

The pressure and skin friction coefficients can be seen in Figure 14, with comparison curves for the data by Galbraith & Visbal[2] and with XFoil.[10] The separation bubble is clearly visible in the skin friction profile, with separation occurring at 24% of the chord.

Table 2 gives the location of separation and reattachment with comparison to previously published results, as well as the transition location and the mean lift and drag coefficients. TU-BS corresponds to the PIV experiments at the Technical University of Braunschweigs Low-Noise Wind Tunnel,[11] while HFWT is for the PIV experiments at the Air Force Research Labs Horizontal Free-Surface Water Tunnel.[3]

Contours of instantaneous and average span-wise vorticity on the plane at the middle of the wing ($y = 0.1$) are shown in Figure 15. Average non-dimensional velocity correlations can be seen in Figure 16, and reveal the transition to turbulence. This is verified by looking at the displacement thickness, momentum thickness, and shape factor of the pseudo-velocity profile (Figure 20). A sharp increase in shape factor reveals that, on the average flow, transition to turbulence occurs at a distance of 0.51 chords from the leading edge. The curve for the shape factor lies in between the XFoil predictions with critical amplification factors of 9 and of 7.5 (dashed and dash-dotted lines respectively in the figure).
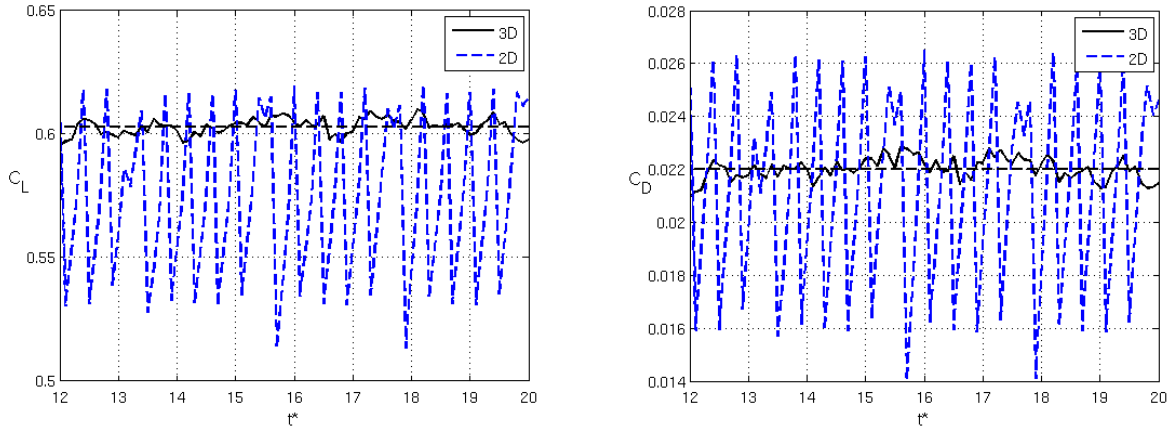
American Institute of Aeronautics and Astronautics

**Figure 12.** Time variation of lift coefficient (left) and drag coefficients (right) at $Re = 60{,}000$: 2D versus 3D simulations.
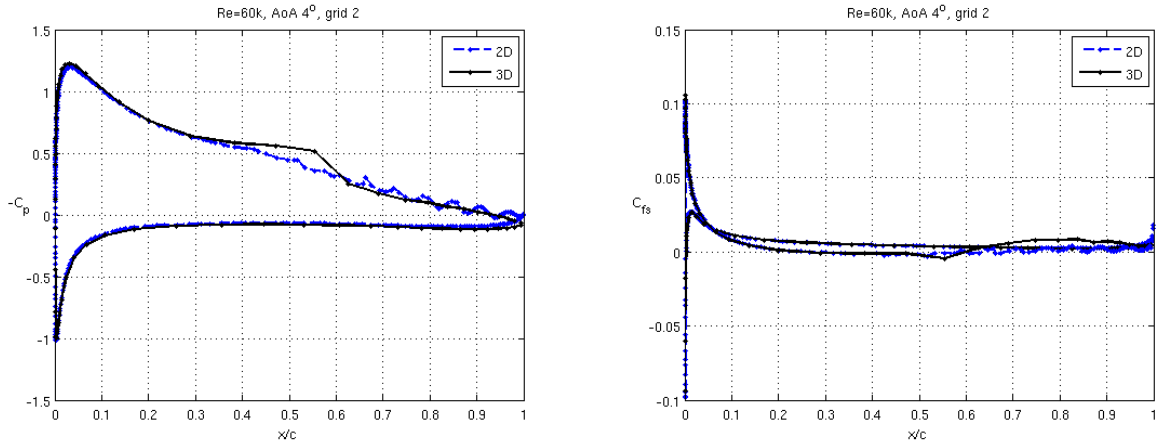


**Figure 13.** Average pressure coefficient (left) and stream-wise skin friction coefficient (right) at $Re = 60{,}000$: 2D versus 3D simulations.

**Table 2.** SD7003 at Reynolds 60,000 and $4°$ angle of attack using grid 2.

| Source | Freestream Turbulence $Tu$ | Separation $x_{sep}/c$ | Transition $x_{tr}/c$ | Reattachment $x_r/c$ | $\overline{C_L}$ | $\overline{C_D}$ |
|---|---|---|---|---|---|---|
| TU-BS[11] | 0.08 % | 0.30 | 0.53 | 0.62 | - | - |
| HFWT[3] | $\sim 0.1\%$ | 0.18 | 0.47 | 0.58 | - | - |
| Visbal[2] | 0 | 0.23 | 0.55 | 0.65 | - | - |
| XFoil[10] | $(N_{crit} = 7.5)$ | 0.26 | 0.57 | 0.60 | 0.5826 | 0.0181 |
| present ILES | 0 | 0.24 | 0.51 | 0.60 | 0.6028 | 0.0220 |

American Institute of Aeronautics and Astronautics
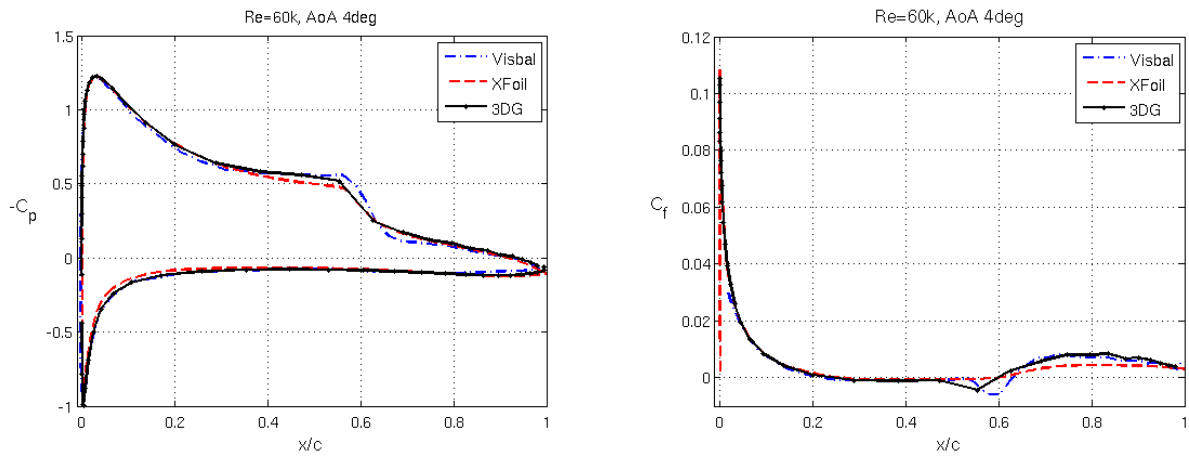
**Figure 14.** Average pressure and stream-wise skin friction coefficients at $Re = 60,000$, with comparison to the computations by Galbraith & Visbal and with XFOIL.
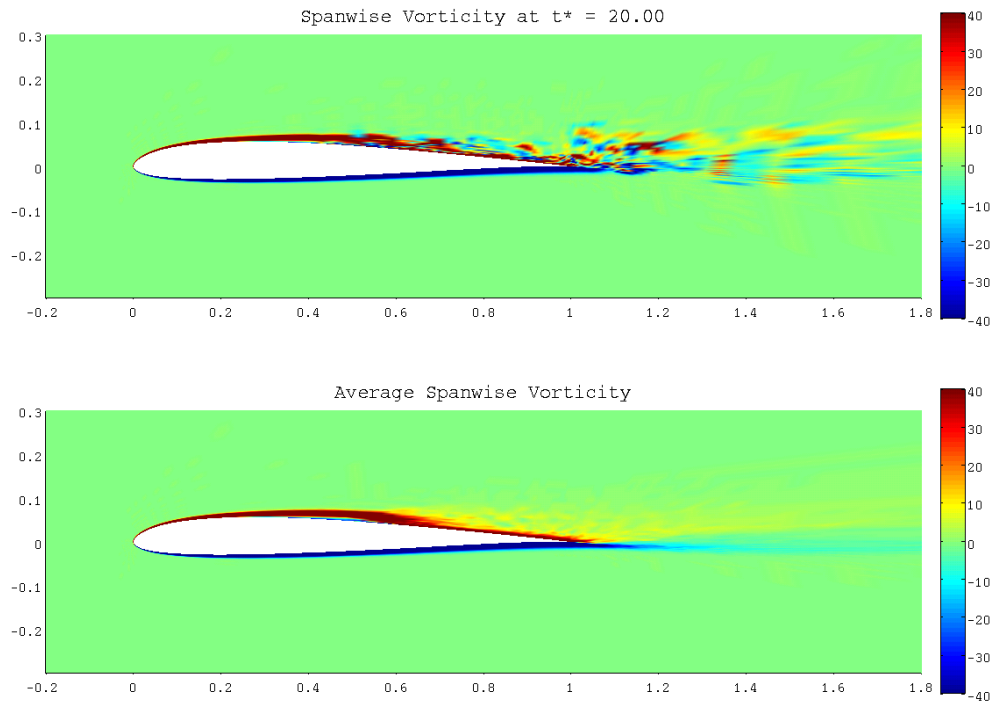


**Figure 15.** Instantaneous (top) and average (bottom) span-wise vorticity on the plane at the middle of the wing at $Re = 60,000$.
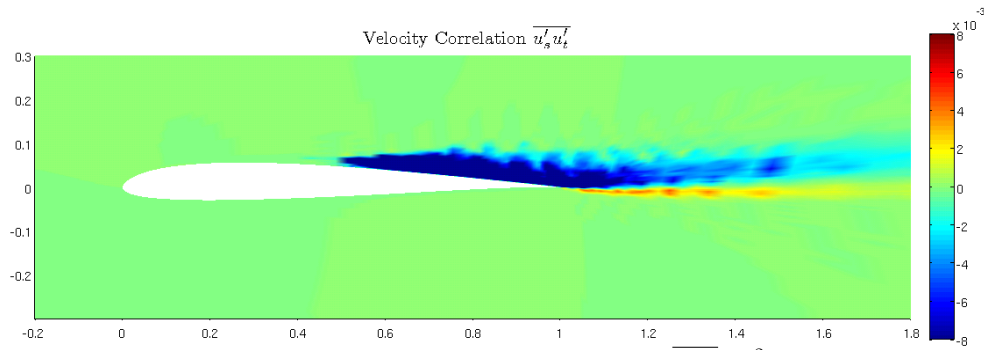


**Figure 16.** Average non-dimensional velocity correlations $\overline{u'_s u'_t} / U_\infty^2$ at $Re = 60,000$.
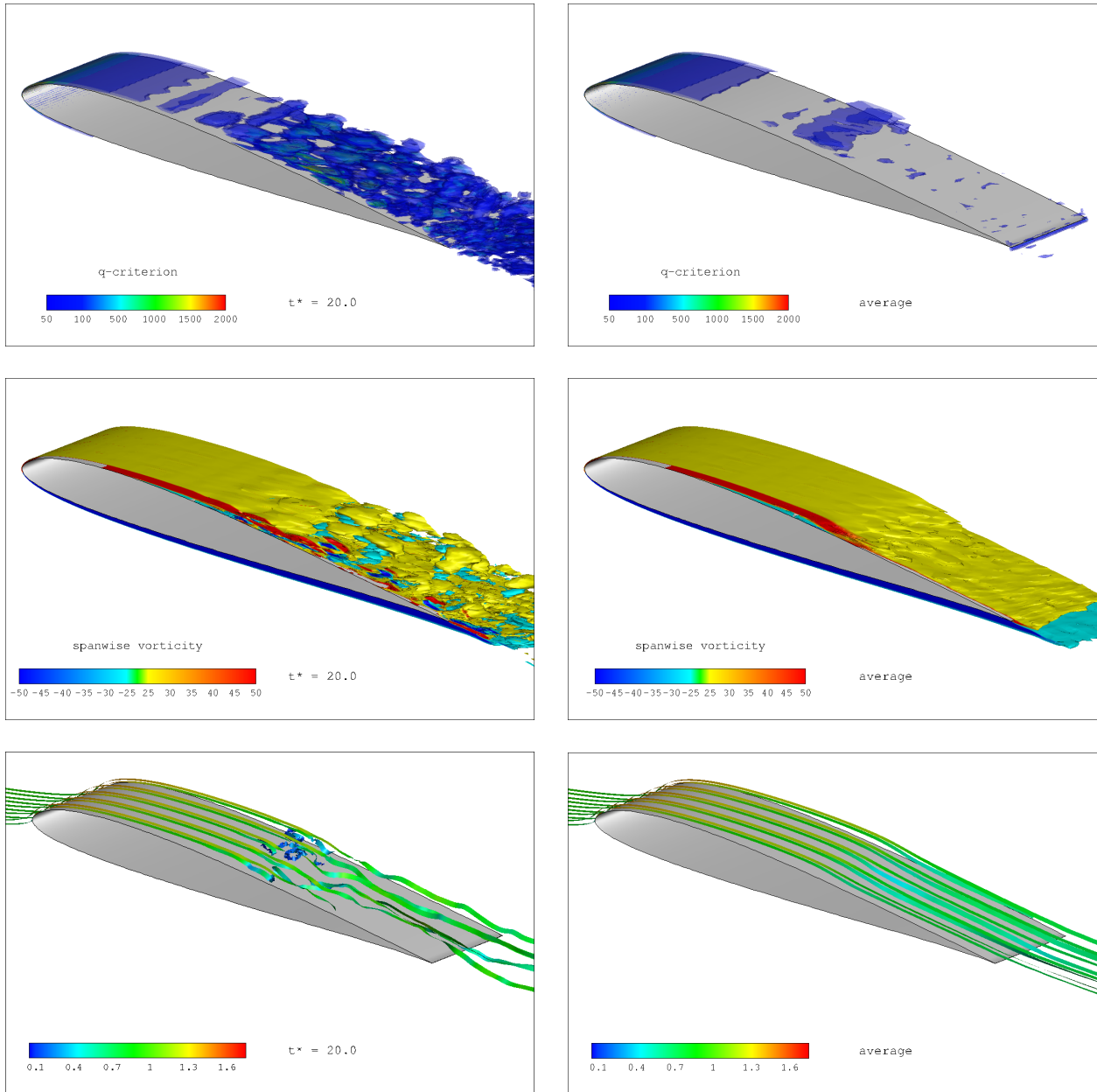
**Figure 17.** Instantaneous (left) and average (right) iso-surfaces of q-criterion (top), span-wise vorticity (middle), and streamlines (bottom) at $Re = 60,000$.
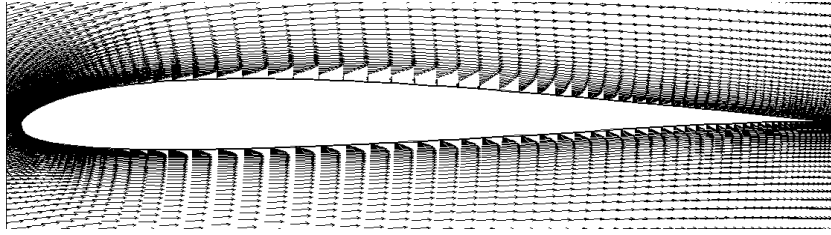
American Institute of Aeronautics and Astronautics

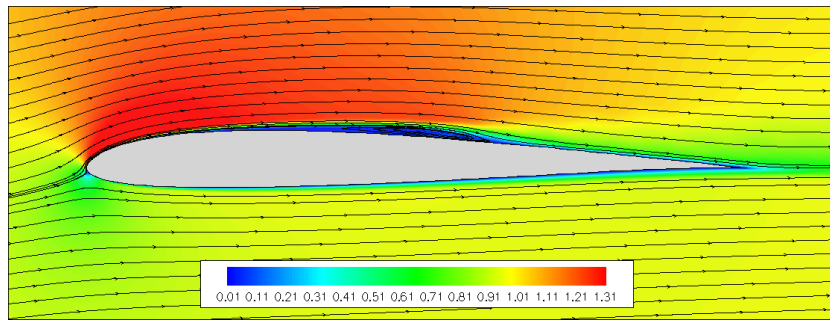**Figure 18. Average velocity vectors on the midplane at $Re = 60{,}000$.**



**Figure 19. Average steamlines on the midplane at $Re = 60{,}000$. The colored contours show velocity magnitude.**
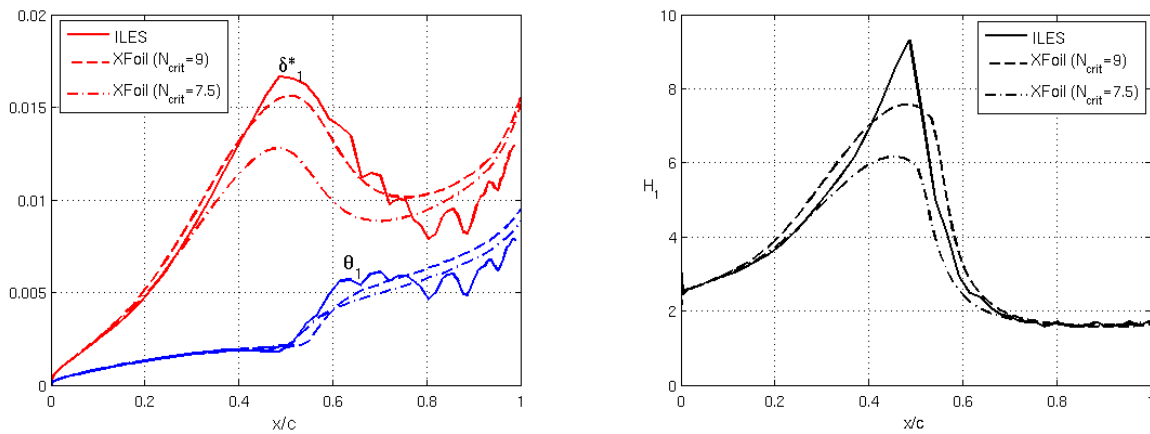


**Figure 20. Boundary layer average displacement and momentum thicknesses (left), and shape factor (right) evolution along the stream-wise direction on the midplane at $Re = 60{,}000$. The dashed and dash-dotted lines show XFoil's predictions with critical amplification factor $N_{crit}$ of 9 and 7.5, respectively.**

American Institute of Aeronautics and Astronautics

## 3. Transition Mechanism

In order to understand the transition mechanism, we look at the fluctuating stream-wise pseudo-velocity

$$u_1^{*'}(\vec{x}, t) = u_1^*(\vec{x}, t) - \overline{u_1^*}(x) ,$$

where the over-line denotes temporal average. Profiles of auto-correlations $\overline{u_1^{*'\,2}}/u_e^2$ can be seen on the left plot of Figure 21, for chord-wise stations $x/c \in [0.1, 0.3]$. Each profile has the shape of a Tollmien-Schlichting (TS) mode, and we observe an increase in perturbation amplitude as the chord-wise location increases.

This is quantified by computing the amplification $A_1$ of stream-wise TS waves at any location $x$, namely

$$A_1(x) = \frac{1}{n_e u_e(x)} \sqrt{\int_0^{n_e} \overline{u_1^{*'\,2}} \, dn} . \tag{18}$$

The amplification factor $N_1$ of the stream-wise perturbations is then

$$N_1(x) = \ln\left(\frac{A_1(x)}{A_{1_0}}\right) \tag{19}$$

in which $A_{1_0}$ is the amplification at the onset of transition, or equivalently
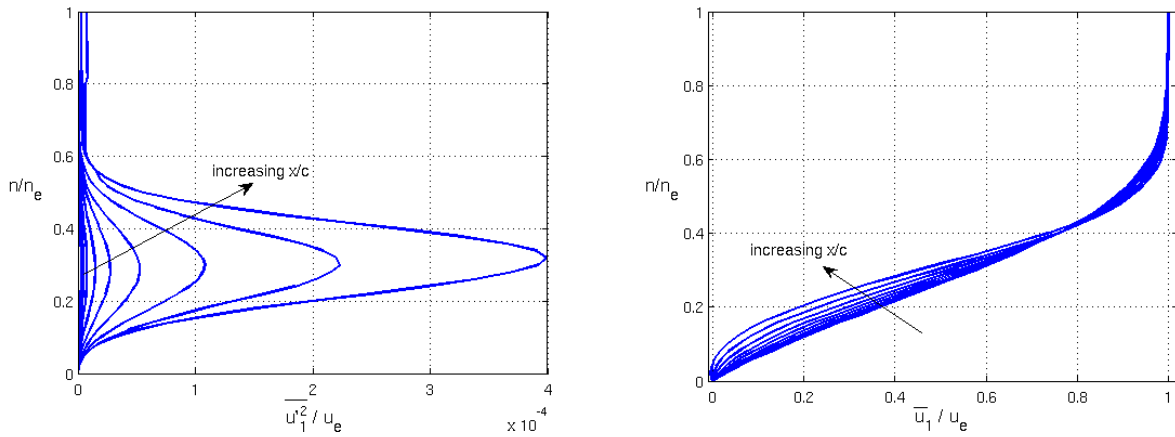
$$e^{N_1} = \frac{A_1(x)}{A_{1_0}} . \tag{20}$$



**Figure 21.  Boundary layer fluctuating stream-wise pseudo-velocity profiles $\overline{\left(u_1^{*'}\right)^2}/u_e$ (left), and average stream-wise pseudo-velocity profiles $u_1^*/u_e$ (right), at different chord-wise locations $x/c \in [0.1, 0.3]$ on the midplane at $Re = 60{,}000$.**
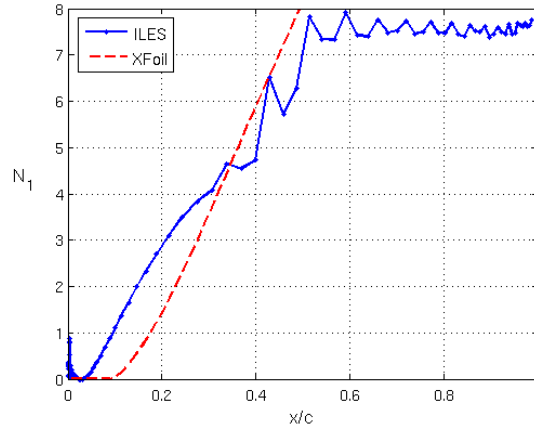


**Figure 22.  Amplification factor $N_1$ of stream-wise pseudo-velocity perturbations for the flow at $Re = 60{,}000$.**

American Institute of Aeronautics and Astronautics

The growth of the stream-wise amplification factor along the chord-wise direction can be seen in Figure 22. The fluctuations observed from the separation location on ($x/c \geq 0.24$) indicate that the temporal average needs to be carried out over a longer period of time. The dotted red line shows the amplification factor of the single most energetic wave as predicted by XFoil, while the blue line is the result of the integration (18) and hence corresponds to the compounded energy of all the waves; this explains why the XFoil line gives a smaller amplification factor at any given location. However, the slopes of the lines from the present simulations and from XFoil are very similar, which suggests that even with the relatively coarse grid used we are able to properly capture unstable modes.

Both the shape of the fluctuating stream-wise pseudo-velocity profiles, and the spatial growth of the amplification factor, indicate that the mechanism of transition for this low Reynolds number flow is a TS transition and not a bypass transition.

## IV.    Conclusions

This paper presents some preliminary results obtained with a discontinuous Galerkin method for the prediction of transition associated with a laminar separation bubble on the SD7003 airfoil. The grid resolution utilized is clearly too coarse to capture all the scales of motion present in the flow, yet it appears to produce a remarkable agreement with results obtained with much finer LES simulation[2] as well as with the results obtained with well-validated codes such as XFoil[10] and experimental data.[3]

The study of the boundary layer fluctuating stream-wise pseudo-velocity profiles and of the spatial growth of the amplification factor shows that the transition taking place at a Reynolds number of 60,000 is due to unstable TS waves.

Our future work will concentrate on validating these results by performing spatial and temporal resolution studies. Further extension will also include the simulation of pitching and heaving airfoils as required for the design of micro-air vehicles. It is known that in these situations the accurate prediction of transition is of crucial importance. For the case of a moving wing, a well-validated time-averaged solver such as XFoil is not available and therefore the use of LES seems to be the only viable option.

## Acknowledgments

## References

[1]Zang, Y., Street, R., and Koseff, J., "A dynamic mixed subgrid-scale model and its application to turbulent recirculating flows," *Physics of Fluids*, Vol. A5(12), 1993, pp. 3186–3196.

[2]Galbraith, M. and Visbal, M., "Implicit Large Eddy Simulaion of low Reynolds number flow past the SD7003 arfoil," *Proc. of the 46th AIAA Aerospace Sciences Meeting and Exhibit, Reno, Nevada, AIAA-2008-225*, 2008.

[3]Ol, M., McAuliffe, B., Hanff, E., Scholz, U., and Kahler, C., "Comparison of laminar separation bubbles measurements on a low Reynolds number airfoil in three facilities," *Proc. of the 35th Fluid Dynamics Conference and Exhibit, Toronto, Ontario, Canada, AIAA-2005-5149*, 2005.

[4]Roe, P. L., "Approximate Riemann solvers, parameter vectors, and difference schemes," *J. Comput. Phys.*, Vol. 43, 1981.

[5]Peraire, J. and Persson, P.-O., "The Compact Discontinuous Galerkin (CDG) method for elliptic problems," *SIAM Journal of Scientific Computing*, Vol. 30, No. 4, 2008, pp. 1806–1824.

[6]Persson, P.-O., "Scalable parallel Newton-Krylov solvers for Discontinuous Galerkin discretizations," *Proc. of the 47th AIAA Aerospace Sciences Meeting and Exhibit, Reno, Nevada, AIAA -2009-606*, 2009.

[7]Persson, P.-O. and Peraire, J., "Newton-GMRES preconditioning for Discontinuous Galerkin discretizations of the Navier-Stokes equations," *SIAM Journal of Scientific Computing*, Vol. 30, No. 6, 2008, pp. 2709–2733.

[8]Alexander, R., "Diagonally Implicit Runge-Kutta methods for stiff O.D.E.'s," *SIAM J. Numer. Anal.*, Vol. 14, No. 6, 1977, pp. 1006–1021.

[9]Dubeif, Y. and Delcayre, F., "On Coherent-vortex Identification in Turbulence," *Journal of Turbulence*, Vol. 1, No. 11, 2000, pp. 1–22.

[10]Drela, M., *XFOIL Users Guide, Version 6.94*, MIT Aeronautics and Astronautics Department, 2002.

[11]Radespiel, R., Windte, J., and Scholz, U., "Numerical and Experimental Flow Analysis of Moving Airfoils with Laminar Separation Bubbles," *AIAA Paper 2006-501*, Jan. 2006.